

Direct Measurement of Topological Properties of an Exceptional Parabola

Weiyan Tang¹, Kun Ding^{2*}, Guancong Ma^{1*}

¹ *Department of Physics, Hong Kong Baptist University, Kowloon Tong, Hong Kong, China*

² *The Blackett Laboratory, Department of Physics, Imperial College London,*

London SW7 2AZ, United Kingdom

*Email: k.ding@imperial.ac.uk, phgcma@hkbu.edu.hk.

Abstract. Non-Hermitian systems can produce branch singularities known as exceptional points (EPs). The topological properties of an EP can involve either the winding of eigenvalues that produces a discriminant number (DN) or the eigenvector holonomy that generates a Berry phase, making them richer than typical degenerate points in Hermitian systems. However, the multiplicity of topological invariants also makes them challenging to investigate experimentally. Here, we study a trajectory of square-root EPs with both theory and acoustic experiments. We obtain both the DNs and Berry phases through the measurement of both eigenvalues and eigenfunctions, which are found distinct for non-homotopic paths. Our findings not only shed light on exotic non-Hermitian topology but also provide a route for the experimental characterization of non-Hermitian topological invariants.

Introduction. —The study of non-Hermitian systems [1–3] followed by their realization in optics and classical waves [4–6] have led to a myriad of intriguing phenomena, such as novel lasing [7–9], coherent absorption [10–12], scattering cancellation [13,14], improved optical sensitivity [15,16], topological power transfer [17–19], etc. These discoveries are underpinned by the exotic properties of an EP [20,21], a branch-point singularity at which complex eigenvalues become identical, and one or more eigenvectors are defective. Interestingly, the manifold in the vicinity of an isolated EP already displays topological properties not found in Hermitian systems. For example, a holonomy around a square-root EP induces the two states exchange [22–24] and a quantized Berry phase of π emerges after two complete cycles [30,31]. Meanwhile, the winding of complex eigenvalues around an EP in exceptional lines can lead to nonzero vorticity that contributes to a topological invariant called a DN [27–31]. These facts show that both eigenvalues and eigenvectors play a critical role in non-Hermitian topological properties [28–30], and also distinguishes the EP from degenerate points in Hermitian systems. When considering multiple EPs or trajectories of EPs, even more exotic topology can emerge.

The fundamental importance of eigenvalues and eigenvectors near an EP implies that their experimental characterizations are crucial for the thorough study its topological properties. However, most attempts so far mainly focused on the study of state exchanges [23,32]. In this work, we present direct and thorough measurements of the

topological properties of a continuous trajectory of square-root EPs by obtaining both the DNs and Berry phases from acoustic experiments. Our results reveal that all EPs on the trajectory are topologically anisotropic, possessing distinct DNs and Berry phases. Our approach produces highly accurate and reliable results and avoids the complication of non-adiabatic transitions encountered in dynamic processes [17,33–35].

Exceptional parabola. —We begin by considering a two-state non-Hermitian Hamiltonian

$$H = (\omega_0 - i\gamma_0)\sigma_0 + H_{EP}, \quad (1)$$

where H_{EP} is

$$H_{EP} = -\kappa_0(1 - \zeta^2)\sigma_1 + i\kappa_0(1 + \Xi)(\sigma_3 - \sigma_0). \quad (2)$$

Here $\omega_0 - i\gamma_0$ is the onsite complex eigenvalue with σ_0 being an identity matrix, σ_j is the j -component of the Pauli matrices of spin-1/2. The term $-\kappa_0(1 - \zeta^2)$ ($\kappa_0 > 0$) represents hopping between the two sites, and it has a quadratic dependence on ζ . The non-Hermiticity is induced by a complex parameter $\Xi = \xi_r + i\xi_i$ and $\zeta, \xi_r, \xi_i \in \mathbb{R}$ constitute the three-dimensional (3D) parameter space, as shown in Fig. 1(a). The eigenvalues of Eq. (1) are

$$\omega_{1,2} = \omega_0 - i\gamma_0 - i\kappa_0(1 + \Xi) \pm \kappa_0\sqrt{(1 - \zeta^2)^2 - (1 + \Xi)^2}. \quad (3)$$

We focus on small values of ζ, ξ_r, ξ_i and retain only the respective terms to the lowest order. Thus the eigenvalues become identical when

$$\zeta^2 + \xi_r + i\xi_i = 0, \quad (4)$$

indicating the emergence of square-root EPs. Equation (4) implies $\zeta^2 + \xi_r = 0$ and $\xi_i = 0$, which means the EPs from a parabola on $\xi_r\zeta$ -plane, as shown by the solid red curve in Fig. 1(a).

The exceptional parabola (EPB) invokes intriguing geometry for the system's manifold. We begin by considering its vertex point at $(\xi_r, \xi_i, \zeta) = (0, 0, 0)$, as marked by the star in Fig. 1(a). It has been shown that this EP is anisotropic in the $\xi_r\zeta$ -plane, displaying distinct singular behaviors when approached from ζ and ξ_r -directions [36]. Here, the EPB resides in a 3D space, making it possible to define two inequivalent paths that encircles the vertex EP, as shown in Fig. 1(a-c). The solid green path is on $\xi_i\xi_r$ -plane, which is punctured by the EPB once, whereas the solid purple path on $\xi_i\zeta$ -plane is tangential to the EPB at the vertex. The eigenvalues evolve differently along these two loops, as shown in the Riemann surfaces in Fig. 1(b, c). Such a difference gives rise to distinct topological properties as will be discussed.

Experimental setup. —Equation (1) can be realized with two coupled acoustic cavities [36,37], as shown in Fig. 1(d). Two identical cuboid cavities with a square cross-section (side length of 44 mm) and a height of 110 mm are filled with air. We use the second-order cavity mode as the onsite orbital (onsite eigenfrequency $\omega_0 = 19,613$ rad/s), which has two nodes in the z -direction and is constant in the xy -plane. The cavities are horizontally connected by small holes introducing evanescent coupling. The resultant eigenmodes are shown in Fig. 1(e), in which the states 1 and 2 are respectively symmetric and anti-

symmetric. To encircle the EP, we need to separately tune all three parameters in Eq. (2). The term $i\kappa_0(1 + \Xi)(\sigma_3 - \sigma_0)$ modifies the onsite eigenfrequency and the loss of cavity B. ξ_r tunes the non-Hermiticity, which is realized by adding acoustic sponges to cavity B. ξ_i introduces detuning and is implemented by adjusting the cavity's volume by the inclusion of putty. To realize ζ that gives the hopping a quadratic dependence, we leverage on the cavity mode's symmetry by noting that the hopping strength is proportional to the local acoustic intensity $I \propto \cos^2\left(\frac{2\pi z}{h}\right) = 1 - \left(\frac{2\pi z}{h}\right)^2 + O\left(\left(\frac{2\pi z}{h}\right)^4\right)$, where $z = 0$ is the mirror plane of the cavities. The hopping strength is tunable by adjusting the location of the holes and has a near-quadratic dependence on z , thus realizing ζ . To achieve this, we drill an array of 23×3 holes on a coupling plate. When only the six holes (two rows) near $z = 0$ are open (Fig. 1(d)), the hopping is maximum with $\kappa_0 = 83.5$ rad, because the local acoustic intensity is the largest. This corresponds to $\zeta = 0$. Other values of ζ is then realized by opening holes at different z .

A small port (radius 2 mm) is opened at the top of both cavities for the excitation by a loudspeaker that is placed on cavity A. They also introduce radiative loss, which contributes to γ_0 in our model. The loudspeaker is driven by a waveform generator (Keysight 33500B). We then insert $\frac{1}{4}$ -inch microphones (PCB Piezotronics 378C10) to the side of the cavities at 14 equally spaced ports (7 for each cavity) for the measurement of spectral responses and acoustic fields inside. The signal is recorded by an oscilloscope (Keysight DSO2024A) for post-processing.

Measurement of the DN. We first investigate the winding of eigenvalues. The eigenvalue Riemann surfaces intersect in the broken phase (Fig. 1(b, c)), leading to a nonzero eigenvalue vorticity $v_{jj'}$, defined as

$$v_{jj'} = -\frac{1}{2\pi} \oint_C \nabla_{\vec{\lambda}} \text{Im}\{\ln[\Delta\omega_{jj'}(\vec{\lambda})]\} \cdot d\vec{\lambda}. \quad (5)$$

Here, $\Delta\omega_{jj'}(\vec{\lambda}) = \omega_j(\vec{\lambda}) - \omega_{j'}(\vec{\lambda})$ wherein j, j' label the states ($j \neq j'$) and C denotes a closed path with $\vec{\lambda}$ being the relevant parameters. Equation (5) can be computed in a stepwise manner

$$v_{jj'} = -\frac{1}{2\pi} \sum_{l=1}^{\mathcal{L}} \text{Im}\left\{\ln\left[\frac{\Delta\omega_{jj'}(\lambda_{l+1})}{\Delta\omega_{jj'}(\lambda_l)}\right]\right\}, \quad (6)$$

where λ_l is the parametric coordinate of the l th step on C . The vorticities then contribute to a DN [29,38]. Our system only has two states, so the DN is simply $\mathcal{V} = v_{12} + v_{21}$, and can be obtained by measuring the eigenvalues $\omega_{1,2}$. We tune the acoustic system along a set parameters defined on an encircling path. At each parametric point, we use two microphones to measure the pressure response spectra. The eigenvalues are then retrieved by using a Green's function method [37,39]. For the green loop (Fig. 1(a, b)), the results are shown in Fig. 2(a, b). In Fig. 2(a), each red (blue) dot represents $\Delta\omega_{12(21)}$ at specific parameters (Lists

of parameters are presented in [39]). Excellent agreement with theory (solid curves) is achieved. We see that the $\Delta\omega_{12}$ (red curves) and $\Delta\omega_{21}$ (blue curves) form a closed loop on the complex frequency plane, as shown by the dashed curves in Fig. 2(a). In Fig. 2(b), the argument of both $\Delta\omega_{12}$ and $\Delta\omega_{21}$ accumulate to a quantized value of π after one complete cycle, indicating $\nu_{12} = \nu_{21} = -0.5$. The DN is thus $\mathcal{V}_{\xi_i\xi_r} = -1$. In contrast, when following the purple loop (Fig. 1(a)), both the red and blue curves return to the respective starting point, as shown in Fig. 2(c, d). This yields a different DN $\mathcal{V}_{\xi_i\xi} = 0$.

Measurement of the Berry phase. In parallel with the DNs, the cyclic variation along the two loops also drives the eigenvectors around the vertex EP, which gives rise to a Berry phase

$$\Theta = i \oint_C d\vec{\lambda} \cdot \langle \psi_j^L(\vec{\lambda}) | \nabla_{\vec{\lambda}} | \psi_j^R(\vec{\lambda}) \rangle, \quad (7)$$

with $|\psi_j^R(\vec{\lambda})\rangle$ and $\langle \psi_j^L(\vec{\lambda})|$ being the right and left eigenvectors. Note that owing to reciprocity, we have $\langle \psi_j^L(\vec{\lambda})| = |\psi_j^R(\vec{\lambda})\rangle^T$. Likewise, Eq. (7) can be discretized as

$$\Theta = - \sum_{l=1}^L \text{Im}[\ln \langle \psi_j^L(\lambda_l) | \psi_j^R(\lambda_{l+1}) \rangle]. \quad (8)$$

Equation (8) not only suits for numerical computations [40] but also offers a viable path to experimentally obtain Θ . Although Berry phase emerges from adiabatic processes, Eqs. (7, 8) suggest that the result does not explicitly depend on time. This removes the requirement of performing a dynamic adiabatic process and all information can be obtained by measuring the stationary-states eigenfunctions. However, because stationary-state measurement involves the independent excitation of the system at different λ_l , the results are inevitably contaminated by arbitrary phase factors. Fortunately, it is possible to eliminate such arbitrary phases by applying a specific gauge to guarantee the parallel transport of eigenfunctions at each step [41]. This method also has the advantage of visualizing the accumulation of Berry phase, which is important for determining the winding of eigenfunctions.

In practice, we first experimentally obtain the eigenfunctions by measuring the field distribution in both cavities at a total of 14 positions, 7 for each cavity (Fig. 1(d)), from which the eigenfunctions are obtained [39]. The arbitrary phase can be identified through the connection $\beta_j(\lambda_{l+1}) = \text{Im}[\ln \langle \psi_j^L(\lambda_l) | \psi_j^R(\lambda_{l+1}) \rangle]$. The phase factor $\beta_j(\lambda_{l+1})$ is then compensated by $|\bar{\psi}_j^R(\lambda_{l+1})\rangle = e^{-i\beta_j(\lambda_{l+1})} |\psi_j^R(\lambda_{l+1})\rangle$. For $l = 1$, $|\bar{\psi}_j^R(\lambda_1)\rangle = |\psi_j^R(\lambda_1)\rangle$, indicating the phase of this point serves as the chosen gauge in the calculation. Repeating this procedure for all $l > 1$ eliminates all arbitrary phases, thus ensuring all neighboring eigenfunctions are locally parallel along the encircling path.

Around the vertex EP, an eigenfunction along the solid green path ($\xi_i\xi_r$ -plane) are shown in Fig. 3(a). We follow the state with two cavities being out-of-phase at the starting point

(Point I-1). Mode exchange occurs near Point I-2, at which the field in cavity B nearly vanishes, implying the mixing of the two states. Starting from Point I-3, the two cavities are in-phase until the completion of one cycle. Then, the second cycle begins with a state (II-1) that is almost identical with the state at I-8 (Fig. 3(a)), followed by a mode switching (II-2) across which the two cavities become out-of-phase and remain until the end of the cycle. Upon the completion of two cycles, the state is restored. However, the two states at I-1 and II-8 clearly have a phase difference of π , which is due the Berry phase. This is further confirmed in Fig. 3(b), showing the accumulated Berry phase is quantized to $\Theta_{\xi_i \xi_r} = -\pi$ in two cycles. In contrast, along the purple path ($\xi_i \zeta$ -plane), the eigenfunction exchanges twice (near I-2 and I-6) and are fully restored in only one complete cycle (Fig. 3(c)). The corresponding Berry phase is $\Theta_{\xi_i \zeta} = 0$ (Fig. 3(d)).

Note that although the parallel-transport gauge is path-dependent and it can affect the values of $\beta_j(\lambda_l)$, the holonomic Berry phase Θ is gauge-invariant as long as the states are restored. We further verify this point by the Wilson-loop method [42], which automatically cancels the arbitrary phases by the sequential product of the connections between neighboring steps. By using the same experimental eigenfunctions, we obtain $\Theta_{\xi_i \xi_r} = -0.9971\pi$ and $\Theta_{\xi_i \zeta} = 1.7 \times 10^{-4}$, which conform excellently with the results of the parallel transport.

Discussion and conclusion. EPs on exceptional structures, such as a ring of EPs spawn from a Dirac point or a Weyl point [43,44], can be anisotropic in that the critical behaviors are different when the EP is approached from different parametric directions [28,36]. Our results unveil that the anisotropy of the vertex EP also manifests in distinct topological invariants. An obvious question is how such multiplicity of topological invariants extends for the system's manifold on which the EPB resides. We remark that the winding should yield the same results as long as the loops are homotopic. For example, in Fig. 1(a), the solid green loop can transform to the dashed green loop by simply sliding along the EPB. In other words, the EPB threads through both loops only once. As a result, they must produce the same DN and Berry phase, which we have confirmed with both theory and experiments [39]. Meanwhile, enlarging the solid purple loop and moving it towards $-\xi_r$ direction produces the dashed purple loop, which encircles two EPs. However, the homotopic equivalence of the two loops dictates that they must produce identical results, which have also been confirmed [39].

More insights can be obtained by examining the discriminant fields, defines as $\vec{D}(\vec{\lambda}) = \nabla_{\vec{\lambda}}[\text{Im} \ln(\Delta)]$, where Δ is the discriminant of $\det(\omega\sigma_0 - H_{EP}) = 0$, *i.e.* the characteristic polynomial of Eq. (2). The results are shown in Fig. 4. For the vertex EP, a vortex is seen on

$\xi_i \xi_r$ -plane but not on the $\xi_i \zeta$ -plane. At $\xi_r = -0.24$, EPB is cut by $\xi_i \zeta$ -plane twice and each intersecting EP carries a vortex with opposite chirality, leading to a zero net vorticity (Fig. 4(c)), which is equivalent to Fig. 4(b). We can then establish that the EPB owes its formation to the fact that all EPs carry the identical vorticity. The last issue worth pointing out is that the eigenvalues and eigenvectors of the H_{EP} span a Hilbert space at each parametric point, and thus constitute a fiber bundle. The DNs and Berry phases are then the consequence of their respective connections defined on this manifold that sustains an EPB. Therefore, the difference between the DNs and Berry phases demonstrates two distinct signatures of their respective holonomy as defined by the green and purple loops.

In summary, we have presented holistic experimental characterizations of two different topological invariants associated with an EPB. Our results also give a unified picture of non-Hermitian topology and confirm the relation between DN and Berry phase [25,45,31]. Our approach offers a route to directly characterize topological invariants without relying on any descendant phenomena such as momentum transfer [46], polarization rotation [47], or bulk-surface correspondence [48].

Acknowledgments. We thank Ruoyang Zhang and Xiaohan Cui for fruitful discussions. This work was supported by Hong Kong Research Grants Council (GRF 12302420, 12300419, ECS 22302718, CRF C6013-18G), National Science Foundation of China Excellent Young Scientist Scheme (Hong Kong & Macau) (11922416) and Youth Program (11802256), and Hong Kong Baptist University (RC-SGT2/18-19/SCI/006). K. D. acknowledges the Gordon and Betty Moore Foundation.

References

- [1] C. M. Bender and S. Boettcher, *Real Spectra in Non-Hermitian Hamiltonians Having P T Symmetry*, Phys. Rev. Lett. **80**, 5243 (1998).
- [2] C. M. Bender, D. C. Brody, and H. F. Jones, *Complex Extension of Quantum Mechanics*, Phys. Rev. Lett. **89**, 270401 (2002).
- [3] C. M. Bender, *Making Sense of Non-Hermitian Hamiltonians*, Rep. Prog. Phys. **70**, 947 (2007).
- [4] R. El-Ganainy, K. G. Makris, M. Khajavikhan, Z. H. Musslimani, S. Rotter, and D. N. Christodoulides, *Non-Hermitian Physics and PT Symmetry*, Nat. Phys. **14**, 11 (2018).
- [5] L. Feng, R. El-Ganainy, and L. Ge, *Non-Hermitian Photonics Based on Parity-Time Symmetry*, Nat. Photon. **11**, 752 (2017).
- [6] M.-A. Miri and A. Alù, *Exceptional Points in Optics and Photonics*, Science **363**, eaar7709 (2019).
- [7] L. Feng, Z. J. Wong, R.-M. Ma, Y. Wang, and X. Zhang, *Single-Mode Laser by Parity-Time Symmetry Breaking*, Science **346**, 972 (2014).
- [8] H. Hodaei, M.-A. Miri, M. Heinrich, D. N. Christodoulides, and M. Khajavikhan, *Parity-Time-Symmetric Microring Lasers*, Science **346**, 975 (2014).
- [9] B. Peng, . K. Ozdemir, S. Rotter, H. Yilmaz, M. Liertzer, F. Monifi, C. M. Bender, F. Nori, and L. Yang, *Loss-Induced Suppression and Revival of Lasing*, Science **346**, 328 (2014).

- [10] Y. Sun, W. Tan, H. Li, J. Li, and H. Chen, *Experimental Demonstration of a Coherent Perfect Absorber with PT Phase Transition*, Phys. Rev. Lett. **112**, 143903 (2014).
- [11] W. R. Sweeney, C. W. Hsu, S. Rotter, and A. D. Stone, *Perfectly Absorbing Exceptional Points and Chiral Absorbers*, Phys. Rev. Lett. **122**, 093901 (2019).
- [12] K. Pichler, M. Kühmayer, J. Böhm, A. Brandstötter, P. Ambichl, U. Kuhl, and S. Rotter, *Random Anti-Lasing through Coherent Perfect Absorption in a Disordered Medium*, Nature **567**, 351 (2019).
- [13] R. Fleury, D. Sounas, and A. Alù, *An Invisible Acoustic Sensor Based on Parity-Time Symmetry*, Nat. Commun. **6**, 5905 (2015).
- [14] E. Rivet, A. Brandstötter, K. G. Makris, H. Lissek, S. Rotter, and R. Fleury, *Constant-Pressure Sound Waves in Non-Hermitian Disordered Media*, Nat. Phys. **14**, 942 (2018).
- [15] H. Hodaei, A. U. Hassan, S. Wittek, H. Garcia-Gracia, R. El-Ganainy, D. N. Christodoulides, and M. Khajavikhan, *Enhanced Sensitivity at Higher-Order Exceptional Points*, Nature **548**, 187 (2017).
- [16] W. Chen, Ş. Kaya Özdemir, G. Zhao, J. Wiersig, and L. Yang, *Exceptional Points Enhance Sensing in an Optical Microcavity*, Nature **548**, 192 (2017).
- [17] J. Doppler, A. A. Mailybaev, J. Böhm, U. Kuhl, A. Girschik, F. Libisch, T. J. Milburn, P. Rabl, N. Moiseyev, and S. Rotter, *Dynamically Encircling an Exceptional Point for Asymmetric Mode Switching*, Nature **537**, 76 (2016).
- [18] H. Xu, D. Mason, L. Jiang, and J. G. E. Harris, *Topological Energy Transfer in an Optomechanical System with Exceptional Points*, Nature **537**, 80 (2016).
- [19] S. Assawaworrarit, X. Yu, and S. Fan, *Robust Wireless Power Transfer Using a Nonlinear Parity–Time-Symmetric Circuit*, Nature **546**, 387 (2017).
- [20] W. D. Heiss, *The Physics of Exceptional Points*, J. Phys. A Math. Theor. **45**, 444016 (2012).
- [21] I. Rotter, *A Non-Hermitian Hamilton Operator and the Physics of Open Quantum Systems*, J. Phys. A Math. Theor. **42**, 153001 (2009).
- [22] C. Dembowski, H.-D. Gräf, H. L. Harney, A. Heine, W. D. Heiss, H. Rehfeld, and A. Richter, *Experimental Observation of the Topological Structure of Exceptional Points*, Phys. Rev. Lett. **86**, 787 (2001).
- [23] C. Dembowski, B. Dietz, H.-D. Gräf, H. L. Harney, A. Heine, W. D. Heiss, and A. Richter, *Encircling an Exceptional Point*, Phys. Rev. E **69**, 056216 (2004).
- [24] Q. Zhong, M. Khajavikhan, D. N. Christodoulides, and R. El-Ganainy, *Winding around Non-Hermitian Singularities*, Nat. Commun. **9**, 4808 (2018).
- [25] A. A. Mailybaev, O. N. Kirillov, and A. P. Seyranian, *Geometric Phase around Exceptional Points*, Phys. Rev. A **72**, (2005).
- [26] S.-Y. Lee, J.-W. Ryu, S. W. Kim, and Y. Chung, *Geometric Phase around Multiple Exceptional Points*, Phys. Rev. A **85**, 064103 (2012).
- [27] D. Leykam, K. Y. Bliokh, C. Huang, Y. D. Chong, and F. Nori, *Edge Modes, Degeneracies, and Topological Numbers in Non-Hermitian Systems*, Phys. Rev. Lett. **118**, 040401 (2017).
- [28] H. Shen, B. Zhen, and L. Fu, *Topological Band Theory for Non-Hermitian Hamiltonians*, Phys. Rev. Lett. **120**, 146402 (2018).
- [29] K. Kawabata, K. Shiozaki, M. Ueda, and M. Sato, *Symmetry and Topology in Non-Hermitian Physics*, Phys. Rev. X **9**, 041015 (2019).
- [30] K. Kawabata, T. Bessho, and M. Sato, *Classification of Exceptional Points and Non-Hermitian Topological Semimetals*, Phys. Rev. Lett. **123**, 066405 (2019).
- [31] L. Li, C. H. Lee, and J. Gong, *Geometric Characterization of Non-Hermitian Topological Systems*

- through the Singularity Ring in Pseudospin Vector Space, *Phys. Rev. B* **100**, 075403 (2019).
- [32] T. Gao, E. Estrecho, K. Y. Bliokh, T. C. H. Liew, M. D. Fraser, S. Brodbeck, M. Kamp, C. Schneider, S. Höfling, Y. Yamamoto, F. Nori, Y. S. Kivshar, A. G. Truscott, R. G. Dall, and E. A. Ostrovskaya, *Observation of Non-Hermitian Degeneracies in a Chaotic Exciton-Polariton Billiard*, *Nature* **526**, 554 (2015).
 - [33] X.-L. Zhang, S. Wang, B. Hou, and C. T. Chan, *Dynamically Encircling Exceptional Points: In Situ Control of Encircling Loops and the Role of the Starting Point*, *Phys. Rev. X* **8**, 021066 (2018).
 - [34] X.-L. Zhang and C. T. Chan, *Dynamically Encircling Exceptional Points in a Three-Mode Waveguide System*, *Commun. Phys.* **2**, 63 (2019).
 - [35] X.-L. Zhang, T. Jiang, and C. T. Chan, *Dynamically Encircling an Exceptional Point in Anti-Parity-Time Symmetric Systems: Asymmetric Mode Switching for Symmetry-Broken Modes*, *Light Sci. Appl.* **8**, 88 (2019).
 - [36] K. Ding, G. Ma, Z. Q. Zhang, and C. T. Chan, *Experimental Demonstration of an Anisotropic Exceptional Point*, *Phys. Rev. Lett.* **121**, 085702 (2018).
 - [37] K. Ding, G. Ma, M. Xiao, Z. Q. Zhang, and C. T. Chan, *Emergence, Coalescence, and Topological Properties of Multiple Exceptional Points and Their Experimental Realization*, *Phys. Rev. X* **6**, 021007 (2016).
 - [38] Z. Yang, A. P. Schnyder, J. Hu, and C.-K. Chiu, *Fermion Doubling Theorems in 2D Non-Hermitian Systems*, *ArXiv:1912.02788* (2019).
 - [39] See Supplemental Materials for the discussion on data processing methods, the detailed system parameters, and the results of encircling two EPs.
 - [40] R. Resta, *Manifestations of Berry's Phase in Molecules and Condensed Matter*, *Journal of Physics: Condensed Matter* **12**, R107 (2000).
 - [41] D. Vanderbilt, *Berry Phases in Electronic Structure Theory: Electric Polarization, Orbital Magnetization and Topological Insulators* (Cambridge University Press, 2018).
 - [42] K. G. Wilson, *Confinement of Quarks*, *Phys. Rev. D* **10**, 2445 (1974).
 - [43] B. Zhen, C. W. Hsu, Y. Igarashi, L. Lu, I. Kaminer, A. Pick, S.-L. Chua, J. D. Joannopoulos, and M. Soljačić, *Spawning Rings of Exceptional Points out of Dirac Cones*, *Nature* **525**, 354 (2015).
 - [44] A. Cerjan, S. Huang, M. Wang, K. P. Chen, Y. Chong, and M. C. Rechtsman, *Experimental Realization of a Weyl Exceptional Ring*, *Nat. Photon.* **13**, 623 (2019).
 - [45] C. Yin, H. Jiang, L. Li, R. Lü, and S. Chen, *Geometrical Meaning of Winding Number and Its Characterization of Topological Phases in One-Dimensional Chiral Non-Hermitian Systems*, *Phys. Rev. A* **97**, 052115 (2018).
 - [46] X. Liu, S. Xia, E. Jajtić, D. Song, D. Li, L. Tang, D. Leykam, J. Xu, H. Buljan, and Z. Chen, *Universal Momentum-to-Real-Space Mapping of Topological Singularities*, *Nat. Commun.* **11**, 1586 (2020).
 - [47] H. Zhou, C. Peng, Y. Yoon, C. W. Hsu, K. A. Nelson, L. Fu, J. D. Joannopoulos, M. Soljačić, and B. Zhen, *Observation of Bulk Fermi Arc and Polarization Half Charge from Paired Exceptional Points*, *Science* **359**, 1009 (2018).
 - [48] M. Z. Hasan and C. L. Kane, *Colloquium : Topological Insulators*, *Rev. Mod. Phys.* **82**, 3045 (2010).

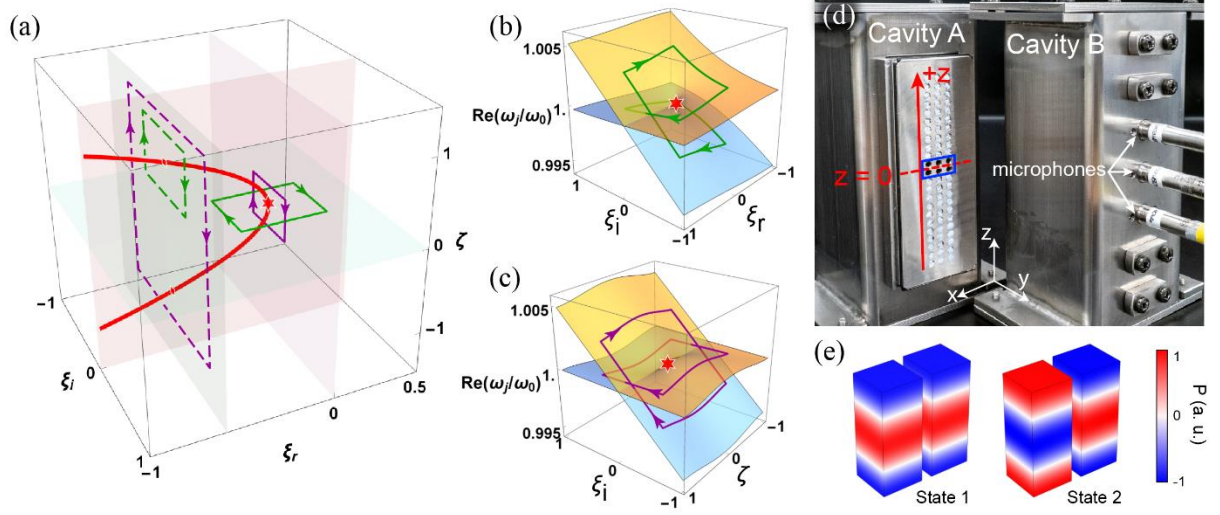


FIG. 1. (a) An EPB (solid red curve) composed of squar-root EPs lies on the $\xi_r\zeta$ -plane ($\xi_i = 0$). The vertex EP is marked by the red star. The green and purple boxes denote different encircling paths. (b, c) show the eigenvalue Riemann surfaces near the vertex EP on the $\xi_i\xi_r$ -plane with $\zeta = 0$ and $\xi_i\zeta$ -plane with $\xi_r = 0$. The paths herein indicate the eigenvalue evolutions along the solid green and purple paths defined in (a). The eigenvalues are normalized by $\omega_0 = 19,613$ rad/s. (d) The experimental setup of the couple acoustic cavities. (e) The two acoustic modes when non-Hermiticity is absent ($(\xi_r, \xi_i) = (-1, 0)$, $\zeta = 0$).

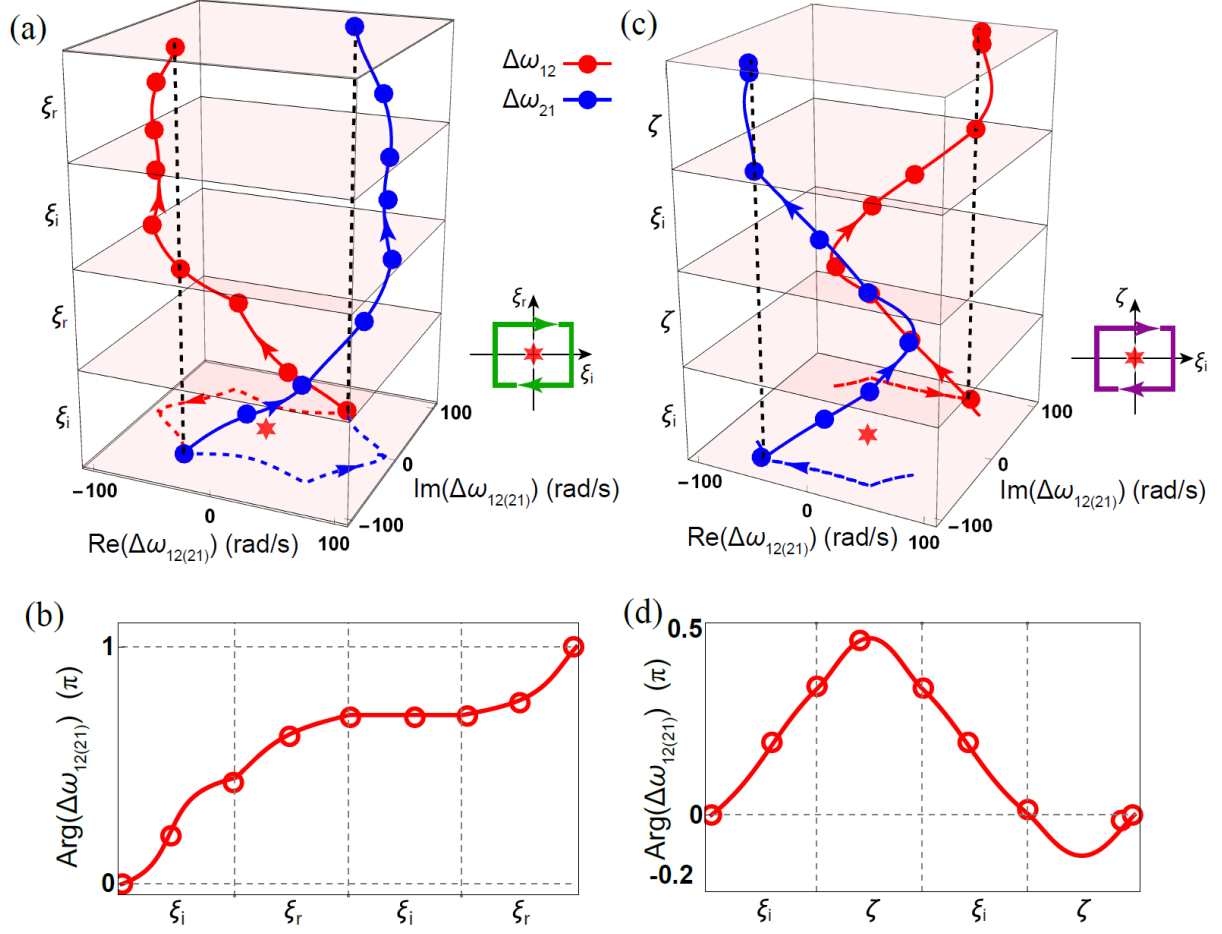


FIG. 2. The evolution of eigenvalue differences $\Delta\omega_{12}$ and $\Delta\omega_{21}$ and their argument changes along the solid green and purple paths are shown in (a, b) and (c, d), respectively. In (b, d), the argument of $\Delta\omega_{21}$ are identical to $\Delta\omega_{12}$, therefore we only show $\Delta\omega_{12}$ by the red lines and dots. Estimated errors are smaller than the marker sizes.

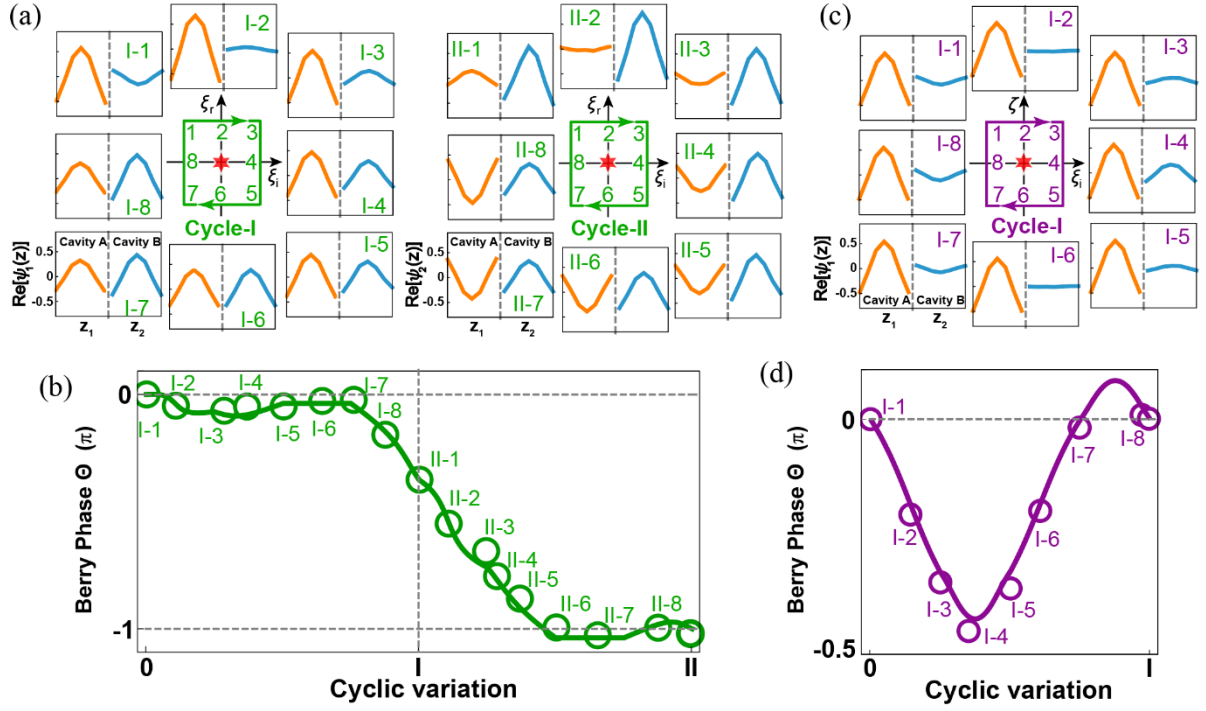


FIG. 3. (a) Measured eigenfunctions (real parts) along the solid green path encircling the vertex EP. The orange and cyan lines respectively denote cavity A and B. (b) The corresponding Berry phase is $-\pi$ after two cycles. (c) Along the solid purple path, the measured eigenfunctions exchange twice near Points I-2 and I-6, and restore themselves in one cycle. (d) The accumulated Berry phase is 0. Markers in (b, d) are experimental results and curves are from theory. Estimated errors are smaller than the marker size in (b, d).

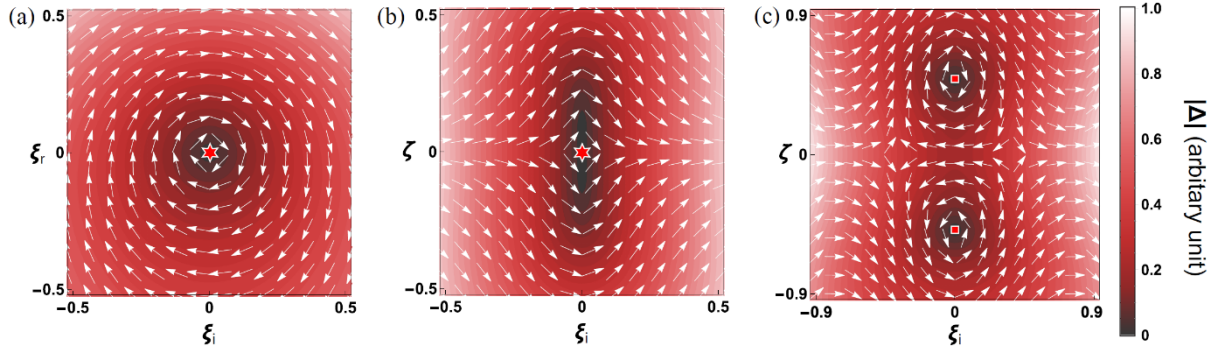


FIG. 4. The discriminant fields \vec{D} (arrows) and the norm of discriminants (color map) near the vertex EP (red stars) on the (a) ξ_r - ξ_i -plane and (b) ξ_i - ζ -plane. A vortex centered at the vertex EP is seen only in (a). (c) When $\xi_r = -0.24$, ξ_i - ζ -plane intersects with the EPB twice at the red squares, around which two vortices with opposite chirality are seen. The length of the arrows are normalized by $|\vec{D}|$.

Supplemental Materials

“Direct Measurement of Topological Properties of an Exceptional Parabola”

Weyuan Tang¹, Kun Ding², Guancong Ma¹

¹ *Department of Physics, Hong Kong Baptist University, Kowloon Tong, Hong Kong, China*

² *The Blackett Laboratory, Department of Physics, Imperial College London, London SW7 2AZ, United Kingdom*

I. Trajectory of the EPs

The eigenvalues of the Hamiltonian H_{EP} is given by

$$\omega_{1,2} = \omega_0 - i\gamma_0 - i\kappa_0(1 + \Xi) \pm \kappa_0 \sqrt{(1 - \zeta^2)^2 - (1 + \Xi)^2}. \quad (1)$$

In the main text, we focus on the region that all three parameters are smaller than 1, so that the higher-order terms under the square root are dropped. Here, we examine the trajectory of the EPs by retaining all the terms. The square-root EPs are found when

$$\zeta^4 - 2\zeta^2 - \xi_r^2 + \xi_i^2 - 2i\xi_i\xi_r - 2\xi_r - 2i\xi_i = 0, \quad (2)$$

which means

$$\zeta^4 - 2\zeta^2 - \xi_r^2 + \xi_i^2 - 2\xi_r = 0, \quad (3)$$

$$\xi_i\xi_r + \xi_i = 0. \quad (4)$$

These two equations give the EP trajectory, which are two exceptional parabolas (EPBs) on the $\xi_r\zeta$ -plane with $\xi_i = 0$ and are symmetric about $\xi_r = -1$. It is noted that the intersections of these two EPBs are two diabolic points at $(\xi_r, \xi_i, \zeta) = (-1, 0, -1)$ and $(-1, 0, 1)$, respectively.

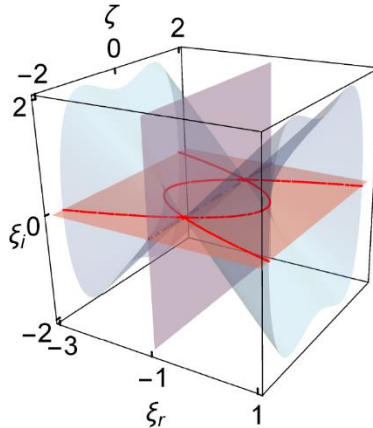


FIG. S1. (a) Eq. (1) yields two EPBs on $\xi_r\zeta$ -plane (with $\xi_i = 0$), which are symmetric about $\xi_i\zeta$ -plane with $\xi_r = -1$. The blue surfaces correspond to the solutions of Eq. (3), and the red planes are solutions to Eq. (4).

II. Retrieval of eigenvalues

We employ the Green's function method [1,2] to obtain the eigenvalues from the measured response spectra. The Green's function is defined as

$$\vec{G}(\omega, \lambda_l) = \sum_{j=1}^2 \frac{|\tilde{\psi}_j^R(\lambda_l)\rangle\langle\tilde{\psi}_j^L(\lambda_l)|}{\omega - \omega_j}, \quad (5)$$

where ω_j denote the eigenvalues with $j = 1, 2$ labeling the eigenstates. $|\tilde{\psi}_j^R(\lambda_l)\rangle$ and $\langle\tilde{\psi}_j^L(\lambda_l)|$ are the normalized biorthogonal right and left eigenvectors, respectively. λ_l represents the parametric coordinates of the l th step along a path, which in our work here, is a loop encircling an EP. Then the pressure responses measured at a specific parameter point λ_l inside the two cavities are given by

$$P(\omega, \lambda_l) = \langle m | \vec{G}(\omega, \lambda_l) | s \rangle, \quad (6)$$

wherein $|s\rangle$ and $|m\rangle$ respectively represent source and microphone. Here, since we excite at the top of cavity A and measure at the central position of the two cavities, $|s\rangle$ and $|m\rangle$ are 2×1 column vectors. By least-square fitting the amplitude of the pressure responses, we can obtain all system parameters: ω_0 , γ_0 , κ_0 , ξ_r , ξ_i , ζ . In this way, the eigenvalues at each parameter point (ξ_r, ξ_i, ζ) along the encircling paths are acquired.

I. Retrieval of eigenfunctions

To obtain the eigenfunctions requires additional information and steps. We note that the eigenfunctions can be expressed as a linear combination of the two onsite modes, *i.e.*,

$$|\psi_j^R(\lambda_l)\rangle = \begin{pmatrix} a_{j,A} |\tilde{\varphi}_A(\lambda_l)\rangle \\ a_{j,B} |\tilde{\varphi}_B(\lambda_l)\rangle \end{pmatrix}, \quad (7)$$

$$\langle\psi_j^L(\lambda_l)| = (b_{j,A} \langle\tilde{\varphi}_A(\lambda_l)|, b_{j,B} \langle\tilde{\varphi}_B(\lambda_l)|), \quad (8)$$

where $|\psi_j^R(\lambda_l)\rangle$ and $\langle\psi_j^L(\lambda_l)|$ are the right and left eigenfunctions of the coupled system, and $|\tilde{\varphi}_{A,B}(\lambda_l)\rangle$ is a column vector representing the normalized onsite eigenmode, *i.e.*, cavity

A or B in isolation. Note that $\langle\tilde{\varphi}_{A,B}(\lambda_l)| = |\tilde{\varphi}_{A,B}(\lambda_l)\rangle^\dagger$, since for a single cavity, the Hamiltonian is Hermitian. Therefore, we first need to obtain the onsite eigenmodes by measuring the spatial distribution of the acoustic field inside the two isolated cavities at each parameter point. Since we employ a longitudinal mode that resonates along the z -axis (Fig. 1(e), main text), we only need to measure both the amplitude and phase at 7 positions along the side boundary of both cavities (Fig. 1(d), main text). The data at a total of 31 frequencies are measured. Then the measured pressure responses are fit using the Green's function

method, which gives

$$P_A(\omega, \lambda_l) = \frac{\langle m | \varphi_A(\lambda_l) \rangle \langle \varphi_A(\lambda_l) | s \rangle}{\omega - (\omega_0 - i\gamma_0)}, \quad (9)$$

$$P_B(\omega, \lambda_l) = \frac{\langle m | \varphi_B(\lambda_l) \rangle \langle \varphi_B(\lambda_l) | s \rangle}{\omega - [\omega_0 - i\gamma_0 - 2i\kappa_0(1 + \Xi)]}, \quad (10)$$

wherein $|m\rangle$ and $|s\rangle$ are now 7×1 column vectors with each element representing the positions of the source (loudspeaker) and the microphone. (Note that since the loudspeaker's position is fixed, there is only one nonzero element in $|s\rangle$.) The onsite eigenfunctions $|\varphi_{A,B}(\lambda_l)\rangle$ are then obtained by numerical fitting both the amplitude and phase of the measured acoustic field in each individual cavity.

Next, we experimentally obtain the acoustic fields in the coupled acoustic cavity system at the same 31 frequencies. For the coupled system, the acoustic field is given by

$$P_j(\omega, \lambda_l) = \langle m | \vec{G}(\omega, \lambda_l) | s \rangle = \sum_{j=1}^2 \frac{\langle m | \psi_j^R(\lambda_l) \rangle \langle \psi_j^L(\lambda_l) | s \rangle}{\omega - \omega_j}. \quad (11)$$

$|m\rangle$ and $|s\rangle$ now become 14×1 column vectors, representing the position of the loudspeaker and microphone. Then, by expressing the eigenfunctions using Eqs. (7, 8), we perform a least-square fitting on the measured data to acquire $a_{j,A}$, $a_{j,B}$, $b_{j,A}$, $b_{j,B}$, thereby obtaining the right and left eigenfunctions $|\psi_j^R(\lambda_l)\rangle$ and $\langle \psi_j^L(\lambda_l)|$. This procedure is repeated for each parameter point $\lambda_l = (\xi_r, \xi_i, \zeta)$ along the encircling loops.

II. Lists of parameters

Here, we present the parameters in our experiments. The second longitudinal mode resonates at $\omega_0 = 19,613$ rad/s. The intrinsic loss of each cavity is $\gamma_0 = 83.5$ rad/s. When $\zeta = 0$ (corresponding to opening six holes (two rows) in the middle ($z = 0$)), the hopping strength is $\kappa_0 = 48.5$ rad/s. In Tables S1 – S4, we list the values of ξ_r, ξ_i, ζ along the four encircling paths that we have investigated (Fig. 1(a), main text).

TABLE S1. The parameters on the solid green loop with $\zeta = 0$.

| Point # | ξ_r | ξ_i |
|---------|---------|---------|
| 1 | 1.06 | -0.28 |
| 2 | 1.08 | 0.00 |
| 3 | 1.06 | 0.36 |
| 4 | 0.56 | 0.37 |
| 5 | 0.02 | 0.37 |
| 6 | 0.01 | 0.01 |
| 7 | 0.01 | -0.26 |
| 8 | 0.55 | -0.28 |

TABLE S2. The parameters on the solid purple loop with $\xi_r = 0$.

| Point # | ζ | ξ_i |
|---------|---------|---------|
| 1 | 0.65 | -0.50 |
| 2 | 0.66 | 0.00 |
| 3 | 0.66 | 0.36 |
| 4 | 0.12 | 0.35 |
| 5 | -0.68 | 0.36 |
| 6 | -0.65 | 0.00 |
| 7 | -0.66 | -0.48 |
| 8 | 0.51 | -0.48 |

TABLE S3. The parameters on the dashed green loop with $\xi_r = -0.24$.

| Point # | ζ | ξ_i |
|---------|---------|---------|
| 1 | 0.53 | -0.29 |
| 2 | 0.51 | 0.00 |
| 3 | 0.54 | 0.49 |
| 4 | 0.41 | 0.51 |
| 5 | 0.02 | 0.51 |
| 6 | 0.02 | 0.01 |
| 7 | 0.03 | -0.29 |
| 8 | 0.36 | -0.29 |

TABLE S4. The parameters on the dashed purple loop with $\xi_r = -0.24$.

| Point # | ζ | ξ_i |
|---------|---------|---------|
| 1 | 0.53 | -0.29 |
| 2 | 0.52 | 0.02 |
| 3 | 0.54 | 0.49 |
| 4 | 0.00 | 0.51 |
| 5 | -0.72 | 0.51 |
| 6 | -0.72 | 0.00 |
| 7 | -0.72 | -0.29 |
| 8 | 0.05 | -0.29 |

III. Discriminant numbers and Berry phases of the dashed loops

Here, we show the results of encircling the EPB with the two dashed loops (Fig. 1(a) in the main text). The dashed green loop encloses one arm of the EPB, whereas the purple dashed loop encloses both arms.

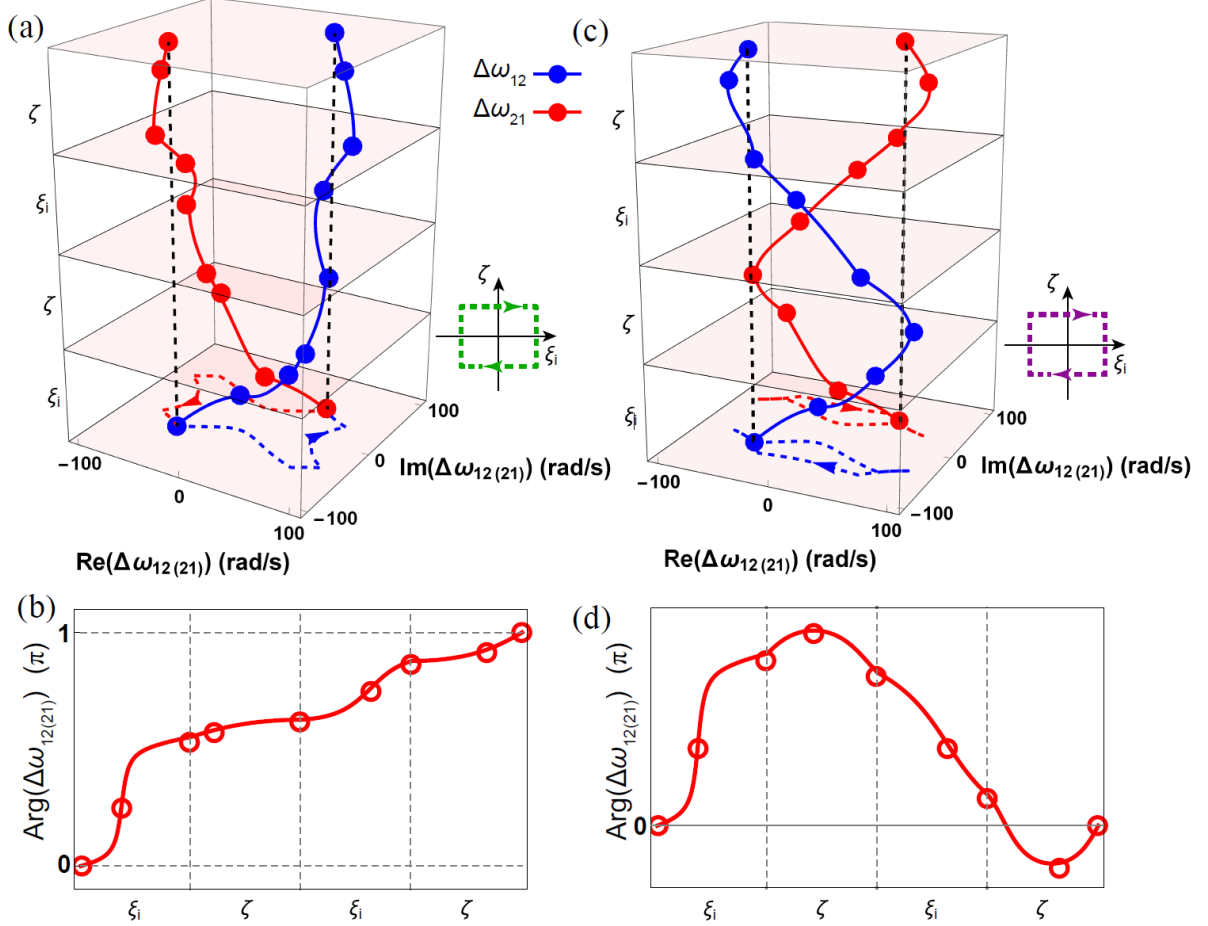


FIG. S2. The evolution of eigenvalue differences $\Delta\omega_{12}$ and $\Delta\omega_{21}$ and their argument changes on the $\xi_i\zeta$ -plane with $\xi_r = -0.24$ along the dashed paths in Fig. 1(a) in the main text. (a) Along the dashed green path, the eigenvalue differences $\Delta\omega_{12}$ and $\Delta\omega_{21}$ form a closed loop and each accumulates a phase of π (b), which yields a discriminant number of -1 . (c) Along the dashed purple path, $\Delta\omega_{12}$ and $\Delta\omega_{21}$ return to their starting points in one complete circle and the accumulated phase is 0 (d). The discriminant number is hence 0. The markers are experimental results, the curves are from theory. In (b, d), $\Delta\omega_{12}$ and $\Delta\omega_{21}$ are identical, therefore the blue curves and markers are covered by the red ones.

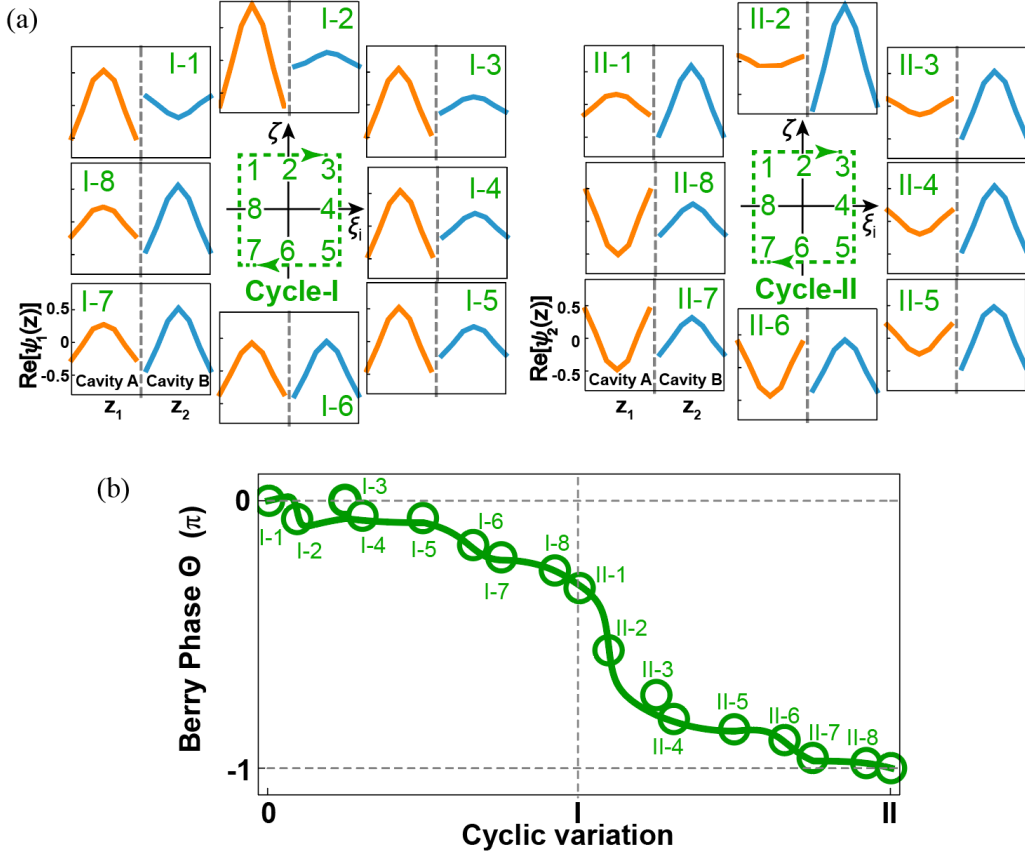


FIG. S3. (a) The measured eigenfunctions (real parts) along the dashed green path encircling the one EP (Fig. 1(a), main text), which lies on $\xi_i\zeta$ -plane with $\zeta = -0.24$. The orange and cyan lines respectively denote cavity A and B. The two eigenfunctions are out-of-phase at their starting point (Point I-1). State exchange occurs near Point I-2 and starting from Point I-3, the two cavities become in-phase until the end of the first cycle. The second cycle begins with a state (II-1) that is the same as the state at I-8. States exchange again near II-2 and the two cavities are out-of-phase again and are restored upon two complete cycles, with a phase difference of π . (b) The corresponding Berry phase is $-\pi$. The markers are experimental results and the curves are from theory.

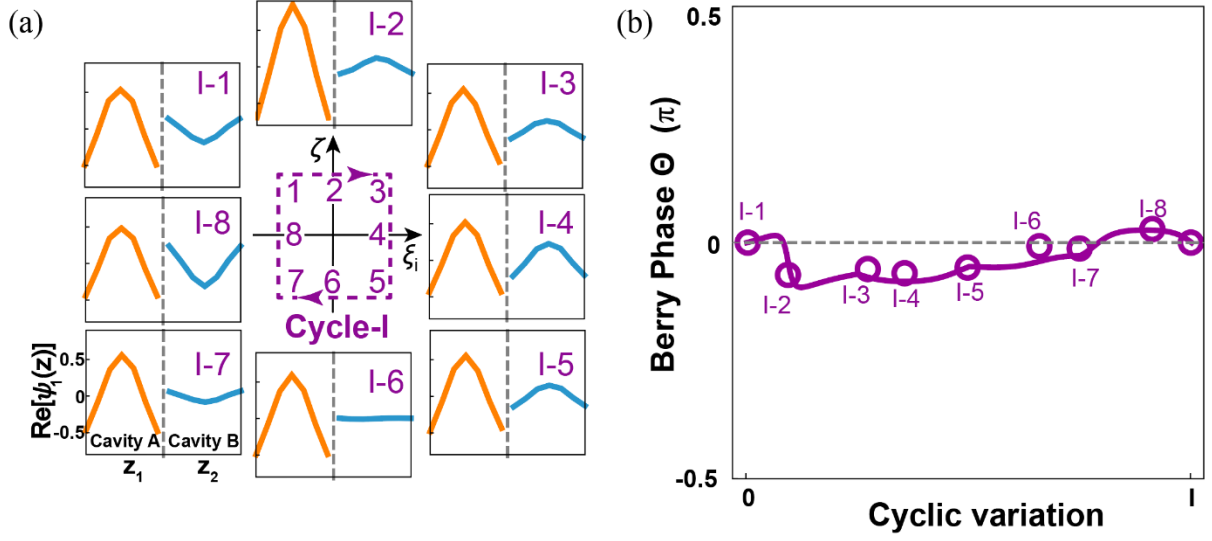


FIG. S4. (a) The measured eigenfunctions (real parts) along the dashed purple path encircling the two EPs, which lies on $\xi_i\zeta$ -plane with $\zeta = -0.24$ (Fig. 1(a), main text). The orange and cyan lines respectively denote cavity A and B. The two wavefunctions are out-of-phase at the starting point (Point I-1). The two states exchange twice near Points I-2 and I-6. The eigenstates are restored at the end of one cycle. (b) The corresponding Berry phase is 0. Markers are experimental results and curves are from theory.

References

- [1] K. Ding, G. Ma, M. Xiao, Z. Q. Zhang, and C. T. Chan, *Emergence, Coalescence, and Topological Properties of Multiple Exceptional Points and Their Experimental Realization*, Phys. Rev. X **6**, 021007 (2016).
- [2] K. Ding, G. Ma, Z. Q. Zhang, and C. T. Chan, *Experimental Demonstration of an Anisotropic Exceptional Point*, Phys. Rev. Lett. **121**, 085702 (2018).